

Phase formation in CrFeCoNi nitride thin films

Smita G. Rao^{1,*}, Boburjon Mukhamedov^{2,*}, Gyula Nagy⁴, Eric N. Tseng¹, Rui Shu¹, Robert Boyd³, Daniel Primetzhofer⁴, Per O. Å. Persson¹, Björn Alling², Igor A. Abrikosov², Arnaud le Febvrier¹, and Per Eklund¹

¹Thin Film Physics Division, Department of Physics, Chemistry, and Biology (IFM), Linköping University, Linköping-58183, Sweden

²Theoretical Physics Division, Department of Physics, Chemistry, and Biology (IFM), Linköping University, Linköping-58183, Sweden

³Plasma and Coatings Physics Division, Department of Physics, Chemistry, and Biology (IFM), Linköping University, Linköping-58183, Sweden

⁴Department of Physics and Astronomy, Uppsala University, Lägerhyddsvägen 1, S-75120 Uppsala, Sweden



(Received 17 November 2022; revised 1 February 2023; accepted 17 March 2023; published 5 May 2023)

As a single-phase alloy, CrFeCoNi is a face centered cubic (fcc) material related to the archetypical high-entropy Cantor alloy CrFeCoNiMn. For thin films, CrFeCoNi of approximately equimolar composition tends to assume an fcc structure when grown at room temperature by magnetron sputtering. However, the single-phase solid solution state is typically not achieved for thin films grown at higher temperatures. The same holds true for Cantor alloy-based ceramics (nitrides and oxides), where phase formation is extremely sensitive to process parameters such as the amount of reactive gas. This study combines theoretical and experimental methods to understand the phase formation in nitrogen-containing CrFeCoNi thin films. Density functional theory calculations considering three competing phases (CrN, Fe-Ni and Co) show that the free energy of mixing, ΔG of $(\text{CrFeCoNi})_{1-x}\text{N}_x$ solid solutions has a maximum at $x = 0.20\text{--}0.25$, and ΔG becomes lower when $x < 0.20$ and $x > 0.25$. Thin films of $(\text{CrFeCoNi})_{1-x}\text{N}_x$ ($0.14 \geq x \geq 0.41$) grown by magnetron sputtering show stabilization of the metallic fcc when $x \leq 0.22$ and the stabilization of the NaCl B1 structure when $x > 0.33$, consistent with the theoretical prediction. In contrast, films with intermediate amounts of nitrogen ($x = 0.22$) grown at higher temperatures show segregation into multiple phases of CrN, Fe-Ni-rich and Co. These results offer an explanation for the requirement of kinetically limited growth conditions at low temperature for obtaining single-phase CrFeCoNi Cantor-like nitrogen-containing thin films and are of importance for understanding the phase-formation mechanisms in multicomponent ceramics. The results from the study further aid in making correlations between the observed mechanical properties and the crystal structure of the films.

DOI: 10.1103/PhysRevMaterials.7.055002

I. INTRODUCTION

Multicomponent and high entropy alloys (HEA) were suggested in the 1980s [1,2] but gained attention in 2004 when two separate studies by Cantor *et al.* (2004) [3] and Yeh *et al.* (2004) [4] showed that alloys with five or more elements in nearly equal ratios can form common crystal structures. The Cantor alloy (CrMnFeCoNi) is among the most-studied high-entropy alloys and exhibits a face centered cubic (fcc) solid solution structure. At the time, it was theorized that the high mixing entropy (ΔS_{mix}) resulted in a low Gibbs free energy (ΔG) which in turn helped in the formation of single-phase solid solutions. This reasoning, however, does

not hold true for all cases, especially when the realm of Cantor alloy-based materials has expanded into new directions [5,6]. Thus, the mechanisms of phase formation and stability in multicomponent alloys remain an important research topic.

Phase prediction in Cantor-based alloys has come a long way since Zhang *et al.* (2008) proposed that the atomic size difference played a role in determining the relative stability phase [7]. The stabilization of a bcc structure with additions of Al into the fcc Cantor alloy is one such example where this theory of atomic size difference comes into play [8,9]. Calculating the valence electron concentration (VEC) is another way to predict stable phases, the concept being that a VEC of ≥ 8 suggests the stabilization of the fcc structure while a VEC of ≤ 6.8 would indicate stabilization of the bcc structure [9]. This understanding is derived from the Hume-Rothery interpretation of VEC, its influence in orbital hybridization and metallic bonding [10]. These methods are relatively straightforward for equiatomic metallic bulk alloys of the 3d and 4d transition metals. However, these methods of phase prediction fail in more complex cases. For example, the VEC rule is valid only if one neglects the presence of multiple phases and irregularities in the composition [11–14]. For ceramic multicomponent systems, one must also take into

*These authors contributed equally to this work.

†Corresponding authors: smita.gangaprasad.rao@liu.se; boburjon.mukhamedov@liu.se

Published by the American Physical Society under the terms of the Creative Commons Attribution 4.0 International license. Further distribution of this work must maintain attribution to the author(s) and the published article's title, journal citation, and DOI. Funded by Bibsam.

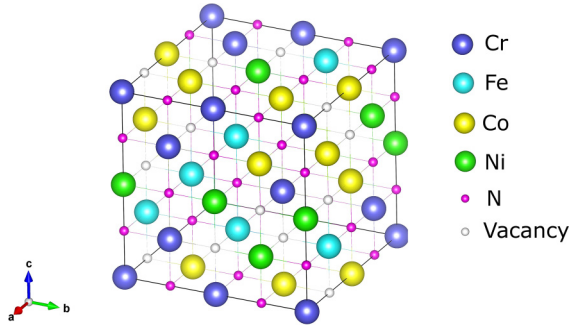


FIG. 1. Schematic representation of $(\text{CrFeCoNi})_{1-x}\text{N}_x$ SQS supercell. The small spheres represent octahedral interstitial positions, partially occupied by N atoms (purple spheres). Empty interstitial positions (vacancies) are shown by white spheres.

consideration the position of the nonmetal atoms in the lattice and the vacancies in the crystal structure [15].

Thin films introduce another level of complexity. Physical vapor deposition techniques such as magnetron sputtering, operate far from thermodynamic equilibrium with limited diffusion, and thus often allow the stabilization of metastable phases, in particular disordered solid solutions. In this work, we combine theoretical and experimental investigations to advance the understanding of the phase formation in thin films of the CrFeCoNi system, a simplified model of the full Cantor alloy. In addition to the metallic system, we consider more complex nitrogen containing multicomponent thin films, addressing the fundamental question of phase formation in the nitrogen-supersaturated and stoichiometric nitride films.

II. METHODS

A. Theoretical methods

Electronic structure calculations of Cr-Fe-Co-Ni alloys with addition of interstitial nitrogen were carried out using the projector augmented-wave method [16] implemented in the Vienna ab initio simulation package (VASP) software [17,18]. Chemical disorder of solid solutions was described using special quasirandom structure (SQS) method [19]. A properly constructed SQS ensures self-averaging of extensive properties of alloys, like the total energy, and therefore does not require the averaging over several configurations: using a single SQS for each concentration is sufficient [20]. Of course, the size of the supercell determines how well it represents the chemical disorder in the simulated system. In our test calculations for nitrogen free equimolar CrCoFeNi alloy we considered the $3 \times 3 \times 3$ and $4 \times 4 \times 4$ supercells with 108 and 256 metal atoms, respectively. The energy difference between the smaller and the larger SQSs was just about 1.4 meV/atom. This indicates that for the systems of interest for this study the constructed SQSs give well converged results. All further calculations were performed for $3 \times 3 \times 3$ fcc supercells (108 metal atoms) with equimolar concentration of metal atoms, i.e., $\text{Fe}_{0.25}\text{Cr}_{0.25}\text{Co}_{0.25}\text{Ni}_{0.25}$. To introduce nitrogen in $\text{Fe}_{0.25}\text{Cr}_{0.25}\text{Co}_{0.25}\text{Ni}_{0.25}$ solid solutions, we considered all octahedral interstitial positions of supercell as a separate “nitrogen-vacancy” sublattice that cannot occupy positions in the metal sublattice (see Fig. 1). By

a vacancy, we mean an empty octahedral position. The amount of N atoms varied depending on its concentration in $\text{Fe}_{0.25}\text{Cr}_{0.25}\text{Co}_{0.25}\text{Ni}_{0.25}$ solid solution. We generated the $(\text{CrFeCoNi})_{1-x}\text{N}_x$ SQSs with six different concentrations of N (mol): $x = 0, 0.1, 0.2, 0.25, 0.35$ and 0.50 , where $x = 0$ was a metal alloy without any nitrogen and $x = 0.50$ corresponded to a stoichiometric nitride with B1 underlying crystal lattice. The ferrimagnetic and paramagnetic cases were considered for the calculations. Magnetic properties were accounted for within a model of collinear local magnetic moments. The magnitudes and orientations of the local moments were calculated self-consistently. The paramagnetic state of $\text{Cr}_{0.25}\text{Fe}_{0.25}\text{Co}_{0.25}\text{Ni}_{0.25}$ solid solution was described within a disordered local moment (DLM) picture [20] implemented in the framework of magnetic SQS method [21]. In the DLM, one can simulate paramagnetic $\text{Cr}_{0.25}\text{Fe}_{0.25}\text{Co}_{0.25}\text{Ni}_{0.25}$ as an effective eight-component alloy $(\text{Cr} \uparrow, \text{Cr} \downarrow)_{0.25}(\text{Fe} \uparrow, \text{Fe} \downarrow)_{0.25}(\text{Co} \uparrow, \text{Co} \downarrow)_{0.25}(\text{Ni} \uparrow, \text{Ni} \downarrow)_{0.25}$ with equal compositions of spin-up and spin-down atoms for each chemically nonequivalent alloy component. The generalized gradient approximation [22] was used to describe the exchange and correlation effects. The cutoff energy for plane waves was set to 450 eV. The convergence criterion for electronic subsystem was set to 10^{-4} eV for subsequent iterations. The full relaxation of SQSs was carried out, which includes the relaxation of supercell volume, shape, and ionic positions. The relaxation of ionic positions was carried out by calculating the Hellman-Feynman forces [23] and the stress tensor and using them in the conjugated gradient method. Relaxation was completed when the forces on the ions became of the order of 10^{-2} eV/Å.

To predict the phase stability of $(\text{CrFeCoNi})_{1-x}\text{N}_x$ solid solutions, we carried out additional calculations of three competing phases, CrN-rich, Fe-Ni-rich, and Co-rich. Our choice of these three reference states was based on the experimental data for films with N content $x \approx 0.20$ – 0.22 , which undergo segregation as discussed below in Sec. III B 2. We tested this segregation trend for all N concentrations in $(\text{CrFeCoNi})_{1-x}\text{N}_x$ SQSs, even though in the experiments there is no segregation in the films with x lower and higher than ~ 0.20 – 0.22 . The details of calculated structures for three competing phases, CrN-rich, FeNi-rich and Co-rich, are available in the Supplemental Material [26] (see Table S2).

The mixing free energy of $(\text{CrFeCoNi})_{1-x}\text{N}_x$ solid solutions at zero pressure is defined as

$$\Delta G = \Delta E - T \Delta S, \quad (1)$$

where ΔE and ΔS denote mixing total energy and mixing entropy which are defined as

$$\begin{aligned} \Delta E(x) = & E\{(\text{CrFeCoNi})_{1-x}\text{N}_x\} - c_1 \cdot E\{\text{Cr}_{1-x_1}\text{N}_{x_1}\} \\ & - c_2 \cdot E\{(\text{FeNi})_{1-x_2}\text{N}_{x_2}\} - c_3 \cdot E\{\text{Co}_{1-x_3}\text{N}_{x_3}\}, \end{aligned} \quad (2)$$

$$\begin{aligned} \Delta S(x) = & S\{(\text{CrFeCoNi})_{1-x}\text{N}_x\} - c_1 \cdot S\{\text{Cr}_{1-x_1}\text{N}_{x_1}\} \\ & - c_2 \cdot S\{(\text{FeNi})_{1-x_2}\text{N}_{x_2}\} - c_3 \cdot S\{\text{Co}_{1-x_3}\text{N}_{x_3}\}, \end{aligned} \quad (3)$$

where c_1 , c_2 , and c_3 denote molar fractions of CrN-rich, FeNi-rich and Co-rich reference phases, and x_1 , x_2 , and x_3 denote the concentration of N in these reference phases. The

proportion of metal atoms in calculated structures is equimolar, therefore $c_1 = 0.25$, $c_2 = 0.5$ and $c_3 = 0.25$. The energies $E\{(\text{CrFeCoNi})_{1-x}\text{N}_x\}$, $E\{\text{Cr}_{1-x_1}\text{N}_{x_1}\}$, $E\{(\text{FeNi})_{1-x_2}\text{N}_{x_2}\}$ and $E\{\text{Co}_{1-x_3}\text{N}_{x_3}\}$ denote the ground state total energies of $(\text{CrFeCoNi})_{1-x}\text{N}_x$ solid solution and three reference phases; and $S_{(\text{CrFeCoNi})\text{N}}$, S_{CrN} , S_{FeNi} and S_{Co} denote their entropies. Since the composition of metals in $(\text{CrFeCoNi})_{1-x}\text{N}_x$ solid solution is equimolar, there is an equal proportion of Fe and Ni in Fe-Ni-rich competing phase. One should note that for each studied N concentration in $(\text{CrFeCoNi})_{1-x}\text{N}_x$ solid solutions, the total amount of N atoms in CrN-, Fe-Ni-rich and Co-rich phases must be equal to the amount of N atoms in $(\text{CrFeCoNi})_{1-x}\text{N}_x$ solid solutions (see Table S2 in Supplemental Material [26]). While calculating the total amount of N in three reference phases it is important to account for the molar fractures of these phases: for CrN-rich, Fe-Ni-rich and Co-rich phases the molar fractures are $c_1 = 0.25$, $c_2 = 0.5$, and $c_3 = 0.25$, respectively. The concentration of N in reference phases will be discussed below.

The entropy of the $(\text{CrFeCoNi})_{1-x}\text{N}_x$ solid solutions and corresponding competing phases was calculated as a sum of configurational S_{conf} and magnetic S_{mag} entropies: $S = S_{\text{conf}} + S_{\text{mag}}$. Both S_{conf} and S_{mag} have been determined within mean-field approximation. The magnetic entropy is nonzero only for paramagnetic alloys, and is defined as $S_{\text{mag}} = k_B \sum_i c_i \cdot \ln(1 + |m_i|)$ [24,25], where m_i is the average magnetic moment of i -th component in the DLM state, and c_i is a concentration of i th component. One should note that configurational entropy in nitrogen containing solid solutions has two contributions: from the disorder in metal sublattice and from the disorder in nitrogen sublattice. More details of calculations for S_{conf} and S_{mag} are available in the Supplemental Material [26].

We considered the isostructural phase separation of $(\text{CrFeCoNi})_{1-x}\text{N}_x$ solid solutions, which means that the Fe-Ni-rich and Co-rich reference phases have fcc lattice and CrN-phase has B1 lattice. The hexagonal closed packed (hcp) lattice for Co was not considered for two reasons: (i) the Co-rich phase may contain iron which stabilizes the fcc lattice of Co [27] and (ii) all the other competing phases and $(\text{CrFeCoNi})_{1-x}\text{N}_x$ solid solution have fcc or B1 structure. For three reference phases, CrN-, Fe-Ni-rich and Co-rich, we generated $3 \times 3 \times 3$ supercells with 108 metal atoms: for Fe-Ni-rich phase, the SQSs with equimolar composition were generated. Table S2 in Ref. [26] shows the number of atoms in the calculated structures for three reference phases. The k -points grid and cutoff energy for plane waves for CrN-, Fe-Ni-rich, and Co-rich phases have been set similar to those for $(\text{CrFeCoNi})_{1-x}\text{N}_x$ SQS's. Full relaxation of supercells for CrN-, Fe-Ni-rich, and Co-rich phases was carried out.

The occupancy of nitrogen in reference phases was prioritized in the following order: first CrN, then Fe-Ni phase and last Co phase. This N distribution among the competing phases was based on the formation energies of mononitrides (see Table S1 in Ref. [26]). According to Table S2 in Ref. [26] at low nitrogen content ($x = 0.10$), the amount of N is not enough to form ideal CrN, therefore $\text{Cr}_{0.69}\text{N}_{0.31}$ with nitrogen deficiency was considered as a competing nitrogen-containing phase while the other two competing phases are considered

TABLE I. Compositions of $(\text{CrFeCoNi})_{1-x}\text{N}_x$ solid solutions and three competing phases.

Nitrogen content x in alloy	Competing phases		
	CrN	Fe-Ni-rich	Co-rich
0.00	—	—	—
0.10	$\text{Cr}_{0.69}\text{N}_{0.31}$	Fe-Ni	Co
0.20	CrN	Fe-Ni	Co
0.25	CrN	$(\text{Fe-Ni})_{0.86}\text{N}_{0.14}$	Co
0.35	CrN	$(\text{Fe-Ni})_{0.67}\text{N}_{0.33}$	Co
0.50	CrN	$(\text{Fe-Ni})\text{N}$	CoN

to stay in their nitrogen-free form: fcc Fe-Ni alloy and fcc Co. At $x = 0.20$, the competing phases are the ideal CrN, and nitrogen-free Fe-Ni and Co. At higher nitrogen content, $x = 0.25$ and $x = 0.35$, the CrN phase cannot accommodate any more N atoms, therefore the surplus nitrogen atoms will occupy the interstitial position in the Fe-Ni-phase. Finally, at the maximum nitrogen content, $x = 0.50$, the competing phases are CrN, $(\text{Fe-Ni})\text{N}$ and CoN. Table I summarizes the chemical compositions of calculated competing phases for each studied concentration of N in the $(\text{CrFeCoNi})_{1-x}\text{N}_x$ solid solutions.

B. Experimental methods

CrFeCoNi metallic and nitrogen-containing thin films were grown on Si(100) substrates by magnetron sputtering from $\text{Cr}_{24}\text{Fe}_{32}\text{Co}_{24}\text{Ni}_{20}$ compound targets (provided by Plansee, Composite Materials GmbH, target thickness = 3 mm and diameter = 50.8 mm) in an ultrahigh vacuum (base pressure $< 9 \times 10^{-7}$ Pa) magnetron sputtering system, described elsewhere [28]. Prior to deposition, the substrates were cleaned with acetone and isopropanol for 10 minutes in an ultrasonic bath and blow-dried with nitrogen gas. The compound target was operated at constant DC power at 100 W (4.9 W/cm^2). Depositions were carried out in an Ar + N₂ atmosphere where the working pressure was set at 0.53 Pa (4.0 mTorr) and the nitrogen content in the films was increased by changing the nitrogen flow ratio for different depositions from 10% to 70% ($\text{N}_2/(\text{Ar} + \text{N}_2)$).

The composition of the films grown was determined by a combination of ion beam analysis techniques. The nitrogen content relative to the cumulative metal content (N/metal) was obtained by time-of-flight-elastic recoil detection analysis (ToF-ERDA). Particle induced x-ray emission (PIXE) was used to resolve the concentration of individual metals (Cr, Fe, Co, Ni). In addition, Rutherford Backscattering Spectrometry (RBS) was used to determine the film thicknesses. Measurements were carried at the 5 MV NEC-5SDH-2 Pelletron Tandem accelerator of the Tandem Laboratory, Uppsala University, Sweden.

ToF-ERDA measurements were carried out using a 36 MeV $^{127}\text{I}^{8+}$ beam. The beam incidence angle on the target was 67.5° , while the gas ionization chamber detector was placed at 45° . Depth profiles of the elemental composition

were acquired from ToF-ERDA time and energy coincidence spectra with the POTKU 2.0 software package [29].

PIXE and RBS measurements were carried out simultaneously, using a beam of 2 MeV He^+ primary ions. The incident angle between the beam and the sample normal was 5° , while the detection angle for RBS was 170° and for PIXE it was 135° . The acquired RBS spectra were evaluated using SIMNRA [30], the PIXE spectra were fitted using the GUPIX code.

X-ray diffraction (XRD) θ - 2θ diffractograms were acquired in a PANalytical X'Pert PRO diffractometer operated using $\text{Cu-K}\alpha$ radiation ($\lambda = 1.54060 \text{ \AA}$) at a voltage of 45 keV and current of 40 mA. All x-ray diffractograms were obtained at room temperature.

Transmission electron microscopy (TEM) and high-resolution TEM (HR-TEM) were carried out on select samples using a FEI Tecnai G2 TF 20 UT instrument operated at 200 kV. The cross-sectional TEM specimens were prepared by manual polishing down to a thickness of 60 μm , followed by Ar^+ ion milling at 5 keV, with a 6° incidence angle, on both sides while rotating the sample in a Gatan precision ion polishing system.

Electron energy loss spectroscopy (EELS) characterization was performed using the Linköping double Cs-corrected FEI Titan3 60–300, operated at 300 kV. Elemental distribution maps were extracted from EELS spectrum images by background subtraction, using a power law, and choosing characteristic edges, N K-edge (402 eV), Cr L_{3,2}-edge (575, 584 eV), Fe L_{3,2}-edge (708, 721 eV), Cr 3₂-edge (779, 794 eV), and Ni L_{3,2}-edge (855, 872 eV) energy loss integration windows.

A scanning electron microscope (SEM), Leo 1550 Gemini, was used for obtaining surface images using the in-lens detector with an acceleration voltage of 8 keV. Backscattered SEM images were acquired using with a Zeiss Gemini 560 instrument fitted with an inlens detector and acquired using an acceleration voltage of 1 kV.

III. RESULTS

A. Density functional theory (DFT) results

The mixing free energy of $(\text{CrFeCoNi})_{1-x}\text{N}_x$ solid solutions was calculated with reference to three competing phases: CrN-rich, Fe-Ni-rich, and Co-rich. We considered the isostructural phase separation of $(\text{CrFeCoNi})_{1-x}\text{N}_x$ solid solutions, as it was mentioned above. Figure 2 shows the configurational and magnetic entropies of mixing of $(\text{CrFeCoNi})_{1-x}\text{N}_x$ solid solutions estimated according to Eq. (3) and Eqs. S1–S3 in Ref. [26]. One should note that contribution to the entropy S_{conf} from “nitrogen-vacancy” sublattice is smaller than the one from metal sublattice, $S_{\text{conf}}^{\text{N}} < S_{\text{conf}}^{\text{Me}}$. Therefore, when nitrogen content is increased, the S_{conf} becomes lower. At $x = 0.50$ the entropy reaches the minimum value, $S_{\text{conf}} = 0.5 \cdot S_{\text{conf}}^{\text{Me}}$, i.e., the solid solution becomes half-ordered. As for the competing phases, CrN has zero configurational entropy except when there is nitrogen deficiency in CrN. The Co-rich phase was considered as pure Co, therefore its configurational entropy is zero. In the Fe-Ni-rich phase there are contributions from metal and nitrogen sublattices.

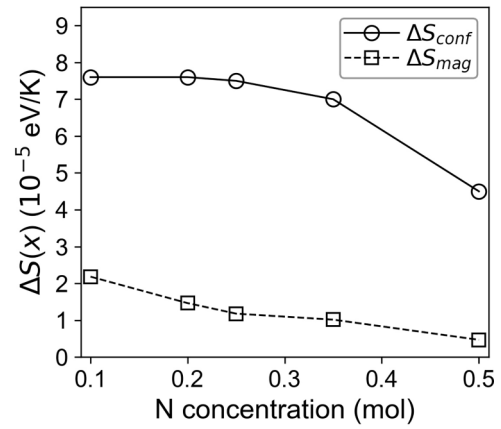


FIG. 2. Mixing entropy of $(\text{CrFeCoNi})_{1-x}\text{N}_x$ solid solutions. The mixing entropy was defined with respect to three reference phases according to Eq. (3).

ties. The latter is present when N content in solid solution $x > 0.20$. However, the entropy of Fe-Ni-rich phase is much smaller compared to one of $(\text{CrFeCoNi})_{1-x}\text{N}_x$ solid solution. Therefore, the resulting configurational entropy of mixing is large enough, $\Delta S_{\text{conf}} \approx 0.87 R$ (7.5 eV/K), which should have a significant stabilization effect at finite temperatures. R denotes the universal gas constant.

To determine the free energy of mixing for paramagnetic alloys we also calculated the magnetic contribution to entropy S_{mag} while considering different magnetic states for reference phases. One should note that for the magnetically ordered structures $S_{\text{mag}} = 0$. For the ferromagnetic $(\text{CrFeCoNi})_{1-x}\text{N}_x$ alloys, the magnetic states of the reference phases are antiferromagnetic CrN with orthorhombic structure, ferromagnetic Fe-Ni and Co; and for the paramagnetic alloys, the references are paramagnetic CrN, ferromagnetic Co and ferromagnetic Fe-Ni at $T = 500 \text{ K}$ or paramagnetic Fe-Ni at $T = 1000 \text{ K}$. The magnetic entropy of mixing ΔS_{mag} of paramagnetic $(\text{CrFeCoNi})_{1-x}\text{N}_x$ solid solution is smaller than ΔS_{conf} as it is shown in Fig. 2. The ΔS_{mag} has a maximum at low N concentration and gradually decreases with increased N in $(\text{CrFeCoNi})_{1-x}\text{N}_x$.

Figure 3 shows the mixing free energy ΔG of $(\text{CrFeCoNi})_{1-x}\text{N}_x$ solid solutions as a function of N concentration. For both ferromagnetic and paramagnetic cases, the ΔG of $(\text{CrFeCoNi})_{1-x}\text{N}_x$ solid solutions demonstrate similar trends, although the ΔG of the ferromagnetic solid solutions is higher. At finite temperatures, the ΔG becomes lower because of entropy factor, therefore one can expect a stabilization of single-phase solid solution with temperature. The $(\text{CrFeCoNi})_{1-x}\text{N}_x$ solid solutions with $x = 0.20$ – 0.25 demonstrate highest ΔG , suggesting that this composition most likely decomposes into three reference phases. At lower and higher N concentrations, the mixing energy becomes lower, i.e., the tendency to segregation becomes weaker.

B. Experimental results

Cantor alloy-based thin films ($\sim 500 \text{ nm}$ thickness) were grown by magnetron sputtering at different deposition temperatures and with different nitrogen contents. The detailed

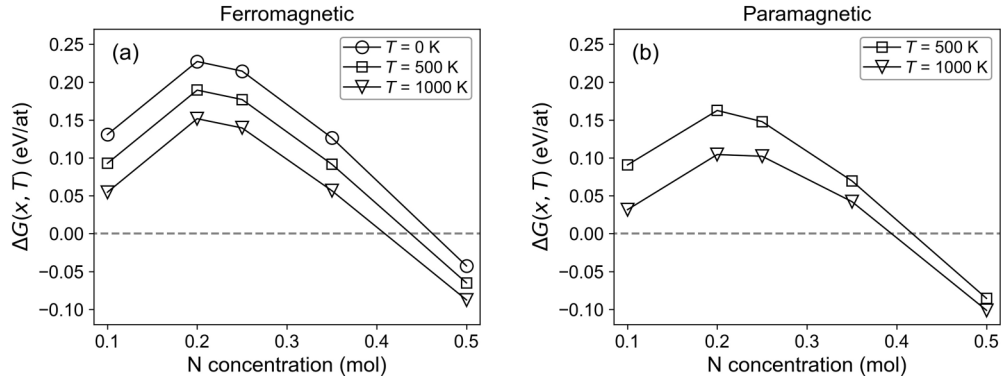


FIG. 3. Mixing free energy of $(\text{CrFeCoNi})_{1-x}\text{N}_x$ solid solutions at (a) ferromagnetic and (b) paramagnetic states. The reference states for the ferromagnetic alloys are antiferromagnetic CrN, ferromagnetic Fe-Ni and Co; and for the paramagnetic alloys, the references are paramagnetic CrN, ferromagnetic Co and ferromagnetic Fe-Ni at $T = 500$ K or paramagnetic Fe-Ni at $T = 1000$ K. The compositions of reference phases are shown in Table I.

composition of both the metallic and nitrogen-containing films acquired from a combination of ERDA and PIXE can be found in the supplementary information (Table S5 and S7, [26]). The nitrogen-containing films will be referred to as $\text{Me}_{1-x}\text{N}_x$ ($\text{Me} + \text{N} = 1$ and with $0.0 \leq x \leq 0.5$).

1. Metallic films ($\text{Me}_{1.0}\text{N}_{0.0}$)

Figure 4 shows the x-ray diffractograms of the metallic films grown at different deposition temperatures starting from room temperature (RT) (i.e., without intentional heating), 200°C , 300°C , and 400°C . The film grown at room temperature is fcc-structured with a (111) texture and a lattice parameter of $3.55 \text{ \AA} \pm 0.02 \text{ \AA}$, comparable to the Cantor alloy (lattice parameter = 3.6 \AA). For the films deposited at higher temperature, the intensity of the fcc (111) peak is reduced and shows asymmetric broadening. The decrease in intensity and the broadening suggest the presence of at least two peaks partially overlapping. This could be an indication of a sec-

ondary orientation or phase [31]. Composition analysis, TEM images, and SEM images of the metallic films along with peak fits of the film grown at 400°C are available in Sec. II of the Supplemental Material (Table S5 and S6, Figs. S1, S2, and S3, Ref. [26]).

2. Nitrogen-containing films ($\text{Me}_{1-x}\text{N}_x$)

Four samples were grown for each deposition temperature at different relative nitrogen flow F_N (10–70%). Detailed compositions are provided in Ref. [26], Table S6. Figure 5 shows the nitrogen content as a function of the deposition temperature for different N_2 flow ratio. For all films, the nitrogen content increased as the nitrogen flow increased from 10 to 70%. For films deposited at room temperature and 200°C , the nitrogen content does not significantly change, however, at higher temperature, the nitrogen content in the film decreased. Hereafter, the samples are referred according to N composition and categorized into four groups: $\text{Me}_{0.86}\text{N}_{0.14}$, $\text{Me}_{0.76}\text{N}_{0.22}$, $\text{Me}_{0.66}\text{N}_{0.34}$, and $\text{Me}_{0.59}\text{N}_{0.41}$, as indicated in

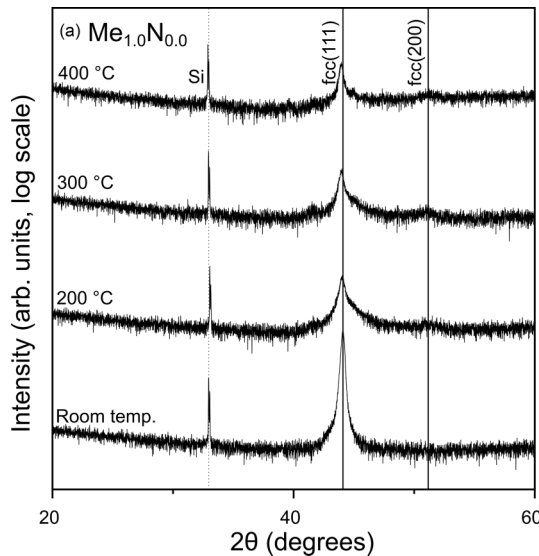


FIG. 4. x-ray diffractograms of CrFeCoNi ($\text{Me}_{1.0}\text{N}_{0.0}$) films grown at different deposition temperature from room temperature to 400°C

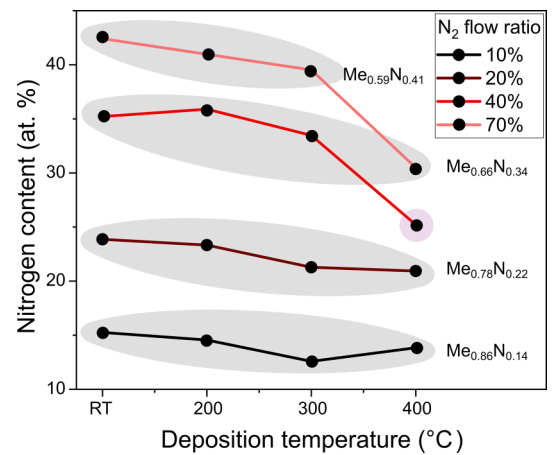


FIG. 5. Variation in nitrogen content of $\text{Me}_{1-x}\text{N}_x$ films for films deposited at different temperature, from room temperature (RT) to 400°C . The composition is an average based on the nitrogen contents of the films contained in a group (indicated in gray). An approximate error bar of ± 1 at.% can be expected for each individual point.

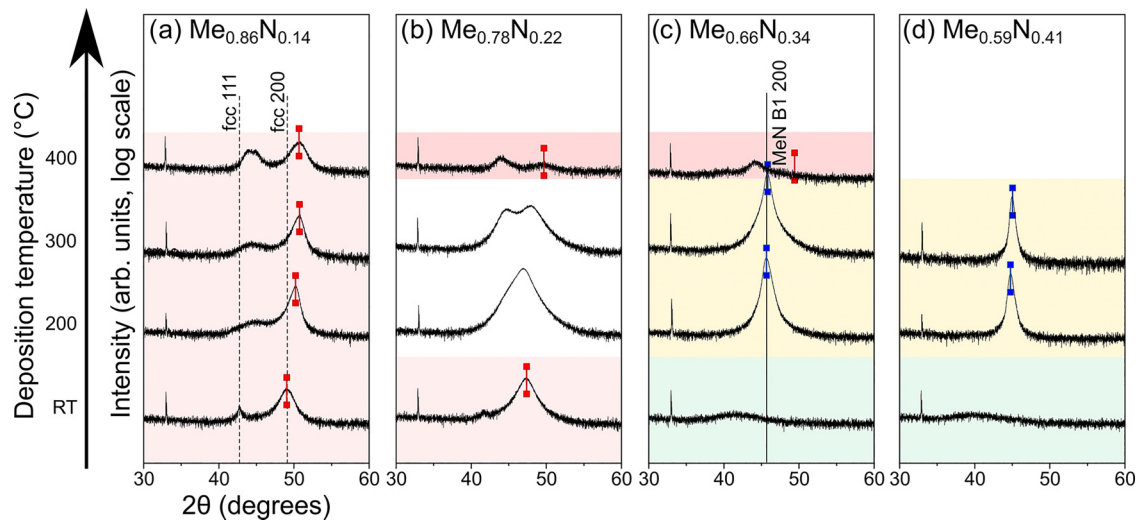


FIG. 6. XRD patterns of CrFeCoNi films with increasing amounts of nitrogen (horizontal axis) and grown at increasing deposition temperatures (vertical axis). Dotted lines in (a) correspond to the fcc 111 and 200 reflections. Peaks marked with red marker correspond to the nitrogen-supersaturated fcc 200 reflections while peaks marked with blue marker correspond to the NaCl-MeN B1 200 reflections. Region shaded in red represents films with fcc structure. Region shaded in yellow represent films with NaCl B1 structure. Region shaded in green correspond to the amorphous films and unshaded region represent the films with multiple phases.

Fig. 5. The film grown at 400 °C and $F_N = 40\%$ is not included as the composition falls in between two groups and the microstructure, crystal structure, and mechanical properties of this film did not differ much from the film grown at $F_N = 70\%$ at the same temperature. More information on surface morphology and x-ray diffractograms of this film is available in Ref. [26] (Fig. S5).

The nitride-formation enthalpy of each of the metals (Cr, Fe, Co, and Ni) plays a large role in phase formation. Among these four metals, Cr has the lowest nitride-formation enthalpy [32], which means that nitrogen would preferentially bond with Cr among the available elements.

Figure 6 shows x-ray diffractograms of the $\text{Me}_{1-x}\text{N}_x$ films where x increases from 0.14 to 0.41 and where each color represents a particular crystal structure. The region shaded in red [low N content/all temperature (T)] in Fig. 6 indicates the films where the stabilization of the fcc is observed ($x = 0.14$). The resulting crystal structure at room temperature is a nitrogen-supersaturated fcc structure with a larger lattice parameter ($\sim 3.87 \text{ \AA}$) in comparison to the Cantor fcc (3.6 \AA). The x-ray diffractograms of these films also indicate a change in texture to 200 in comparison to the 111 textured metallic film. When the deposition temperature is higher, a shift in the XRD peaks to higher angles is observed which implies a decrease of the lattice parameter to approximately 3.65 \AA . At the highest deposition temperature of 400 °C, the x-ray diffractograms show the presence of an additional peak at an approximate 2θ value of 45° , which could belong to a secondary phase. This nitrogen supersaturated fcc structure is retained up to a nitrogen content of $x = 0.22$ [Fig. 6(b)]. The film grown at room temperature exhibits a larger lattice parameter (3.96 \AA). The region shaded in dark red (intermediate N content/high T) in Figs. 6(b) and 6(c) represents the films which also crystallize in the metallic fcc structure despite the higher percentage of nitrogen in the plasma during

growth. The higher deposition temperature may be a reason for the reduced nitrogen contents in the film in comparison to the other films belonging to the $\text{Me}_{0.66}\text{N}_{0.34}$ series. The x-ray diffractograms of the films with $x > 0.22$ indicate a stabilization of CrN isotype [Figs. 6(c) and 6(d), region shaded in yellow (high N content/intermediate T)]. These films are in a nearly stoichiometric nitride phase with a 200 texture. This structure will be referred to as MeN B1. The lattice parameter of the MeN B1 was calculated to be $4.16 \pm 0.02 \text{ \AA}$. Pole figures along with grazing incidence XRD (GIXRD) scans of $\text{Me}_{0.59}\text{N}_{0.41}$ providing further evidence of the NaCl B1 structure can be found in Fig. S6 in Ref. [26].

The diffractograms shaded with green (high N content/RT) on Figs. 6(c) and 6(d) indicate the amorphous films. These films were grown at room temperature with the highest amounts of nitrogen ($x = 0.34$ and 0.41). This region indicates the limit in solubility of nitrogen into the metallic fcc lattice.

From the x-ray diffractograms presented in Fig. 6(b), the unshaded region (intermediate N content/intermediate T) represents the films $\text{Me}_{0.78}\text{N}_{0.22}$ grown at 200 °C and 300 °C. The XRD patterns of these films show complex features with broad asymmetric peaks where several peaks of diffraction are expected indicating towards the presence of multiple phases. In order to further investigate the phase evolution with nitrogen addition, TEM analysis was carried out on the films grown at 300 °C.

Figure 7 shows the bright field TEM (BF-TEM) cross sections of the films grown at 300 °C along with their corresponding high-resolution TEM (HRTEM) and selected area electron diffraction (SAED) patterns. The BF-TEM images show a similar columnar structure for all the nitrogen-containing films [Figs. 7(a)–7(d)]. The SAED patterns of all films shown in Figs. 7(i)–7(l) can be indexed to a cubic structure with increasing lattice parameters which suggests

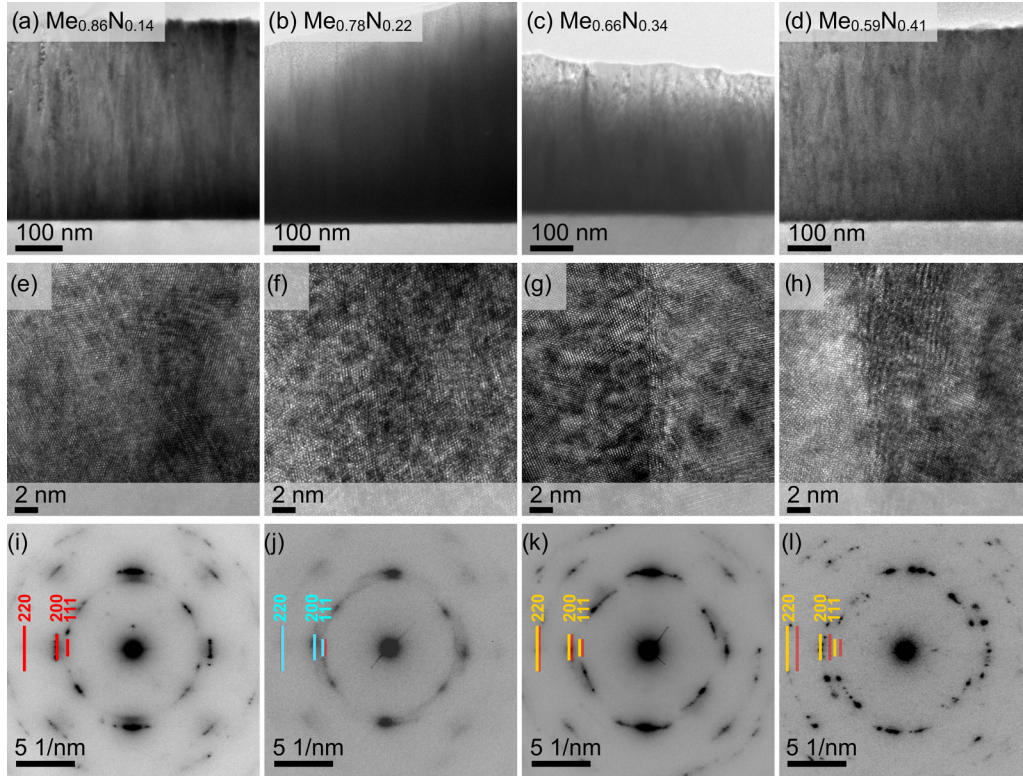


FIG. 7. (a)–(d) BF-TEM cross section images of nitrogen containing films deposited at 300 °C, corresponding HRTEM (e)–(h) and SAED patterns (i)–(l). Red marker lines in (i) indicate the position of reflections from the (111), (200), and (220) planes of the fcc structure. The blue and yellow markers in (j), (k), and (l) indicated the positions of the indexed plane reflections while the red markers indicated the position of the (111), (200), and (220) plane reflections of the nitrogen supersaturated fcc as depicted in (i).

the expansion of the crystal lattice with the incorporation of nitrogen. This is also observed in the x-ray diffractograms where a shift in the peaks to smaller angles is observed (Fig. S4 [26]). The films are preferentially oriented along the 200 and misoriented in the in-plane direction in the case of $\text{Me}_{0.86}\text{N}_{0.14}$. As the nitrogen content is increased [Fig. 7(l), $\text{Me}_{0.58}\text{N}_{0.41}$] the preferential orientation is reduced, the grain size increases, and the diffraction spots are more extended suggesting towards more randomly oriented grains.

The SAED pattern of the $\text{Me}_{0.78}\text{N}_{0.22}$ [Fig. 7(j)] indicates a single-phase solid solution, but the x-ray diffractogram along with scanning TEM-EELS elemental mapping suggests the presence of multiple phases/segregation [Fig. 6(b) and Fig. 8]. This inconstancy is because segregation occurs at a nanoscale while the SAED patterns are acquired at a micron scale.

The EELS map shows the accumulation of the respective element in yellow. For example, in Fig. 8(b), the yellow represents the areas where N is found, while the regions where N is deficient are shown in green, blue, and black. Similarly, in Fig. 8(c) we observe the accumulation Cr in the same region where N was seen to be accumulated in Fig. 8(b). Co on the other hand is seen to be accumulated in the regions where the Cr and N edge signals are not detected [Fig. 8(e)]. The EELS maps therefore suggest the inhomogeneous elemental distribution in the thin film.

Theoretical estimations of the free energy (see Fig. 3) show that, in both the ferromagnetic and the paramagnetic

cases, the ΔG plots show similar trends with the maximum at $x = 0.20$ – 0.25 , although the ΔG of the ferromagnetic solid solutions are higher. The experimentally observed segregation in $\text{Me}_{0.78}\text{N}_{0.22}$ films agree well with calculations, where the solid solutions with $x = 0.20$ – 0.25 demonstrate highest ΔG . These observations also suggest that the samples with this composition decompose into the three reference phases. In $\text{Me}_{0.78}\text{N}_{0.22}$ films deposited at room temperature; segregation can presumably be constrained due to low diffusion rates. At intermediate deposition temperatures, 200 °C and 300 °C, diffusion is more significant, and the thermodynamic factor (high ΔG) enables segregation in the $\text{Me}_{0.78}\text{N}_{0.22}$ films. Finally, at 400 °C, the entropy factor ΔS_{mix} can stabilize a single-phase solid solution structure in $\text{Me}_{0.78}\text{N}_{0.22}$ films.

At $x = 0.10$, the mixing free energy is lower, but still positive. This is because the CrN-reference phase is deficient with nitrogen (see Table I), subsequently making it energetically less favorable than the ideal CrN phase. As a result, in solid solutions with $x < 0.20$ one can expect a stabilization of single-phase structure. At higher nitrogen concentrations, $x > 0.20$, the solid solutions also demonstrate lower ΔG (see Fig. 3). This can be related to the fact that, according to our assumption on the segregation trend, the CrN phase cannot accommodate more nitrogen and the remaining nitrogen atoms are taken by Fe-Ni- and Co-rich reference phases. This, in turn, can be energetically less favorable because the Fe-N, Ni-N and Co-N bonds are weaker than Cr-N bond. As a result, at higher N concentrations the ΔG becomes lower

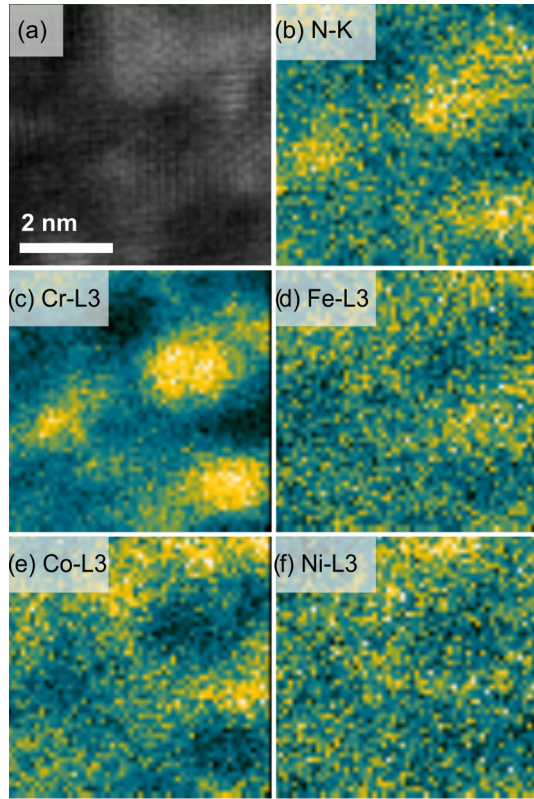


FIG. 8. (a) EELS spectrum image of $\text{Me}_{0.78}\text{N}_{0.22}$ grown at 300°C along with corresponding elemental maps (b)–(f). Yellow corresponds to the edge signal from the respective metal.

and one should expect stabilization of a single-phase structure in $\text{Me}_{1-x}\text{N}_x$ solid solutions. Note that, in Fig. 3, we are only analyzing the ΔG trends to qualitatively explain phase formation in experimental films, without making any direct

comparison between theoretical and experimental transition temperatures (when ΔG becomes zero). There are two reasons for this: (i) samples with $x = 0.14$ and $x = 0.34$ of N which do not decompose, and which have $\Delta G > 0$ (see Fig. 3) can still be metastable single-phase solid solutions; (ii) chemical compositions of experimental $\text{Me}_{1-x}\text{N}_x$ films are not equimolar while the ΔG calculations were performed for equimolar composition.

Figure 9 shows top-view SEM images of the nitrogen-containing films with the deposition temperature increasing along the y axis and nitrogen content increasing along the x axis. Focusing on the films grown at 300°C , the nitrogen supersaturated $\text{Me}_{0.86}\text{N}_{0.14}$ film shows a flakelike morphology [Fig. 9(c)]. As the nitrogen content is increased, a large change in morphology is observed where the appearance of a secondary grain population is observed. This result is consistent with the x-ray diffractogram of $\text{Me}_{0.78}\text{N}_{0.22}$ [Fig 6(b)] where broad asymmetric peaks are observed corresponding to multiple phases. As the nitrogen content is further increased and the MeN B1 is stabilized, the films display large grains [Figs. 9(k) and 9(o)]. The 200-texture observed in the x-ray diffractograms of $\text{Me}_{0.66}\text{N}_{0.34}$ is also visible in the SEM image of the film [Fig. 9(k)].

Table II shows the hardness and reduced Young's modulus of the nitrogen-containing MeN-series thin films. Films with the same crystal structures display similar hardness and modulus values, such that all the films stabilized as an fcc phase show hardness near 15.0 ± 2.0 GPa. The highest hardness was observed in the multiphase samples belonging to the $\text{Me}_{0.78}\text{N}_{0.22}$ group of films. The increase in hardness is consistent with the nanocompositelike structure of the film. Resistivity values of the films are also provided in Table II. The trends indicate that the resistivity is influenced largely by the nitrogen content in the films and less by the crystal structure itself unlike the hardness and modulus.

TABLE II. Hardness and reduced Young's modulus values of nitrogen-containing films obtained from nanoindentation in load-controlled mode.

Film	Deposition temperature ($^\circ\text{C}$)	Structure	Hardness (± 2 GPa)	Reduced Young's modulus (± 10 GPa)	Resistivity ($\pm 5 \mu\Omega\cdot\text{cm}$)
$\text{Me}_{0.86}\text{N}_{0.14}$	RT	fcc	15.5	294	156
	200	fcc	17.0	238	160
	300	fcc	15.8	238	140
	400	fcc	14.9	238	118
$\text{Me}_{0.78}\text{N}_{0.22}$	RT	fcc	14.9	284	159
	200	Multiphase	27.8	284	140
	300	Multiphase	21.9	277	127
	400	fcc	14.1	233	115
$\text{Me}_{0.66}\text{N}_{0.34}$	RT	Amorphous	16.0	267	177
	200	MeN B1	22.1	301	178
	300	MeN B1	20.7	270	168
	400	fcc	14.0	251	202
$\text{Me}_{0.59}\text{N}_{0.41}$	RT	Amorphous	15.6	248	194
	200	MeN B1	22.2	309	196
	300	MeN B1	25.6	272	196

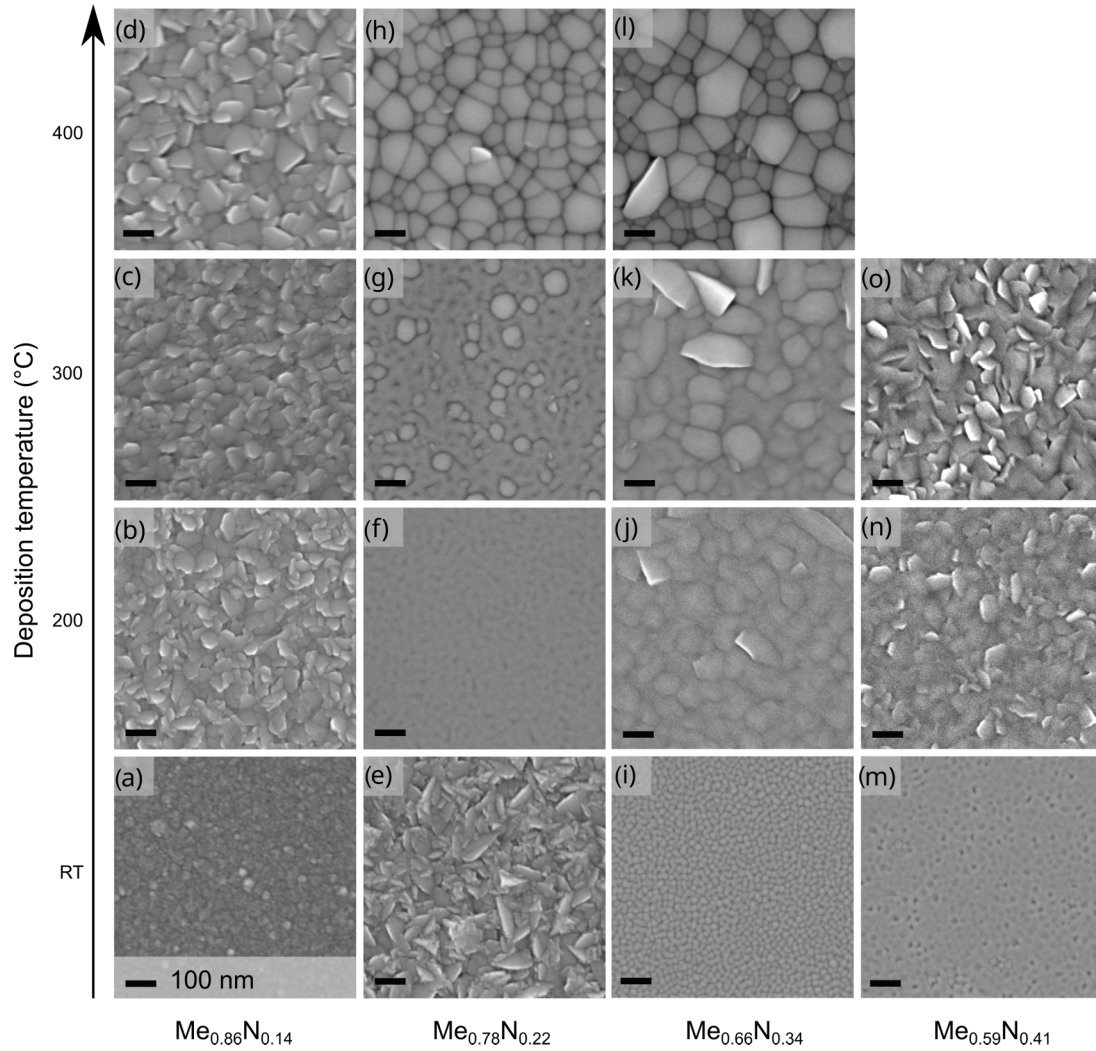


FIG. 9. Top-view SEM images of nitrogen-containing films showing the change in morphology for different nitrogen content and deposition temperature.

IV. CONCLUSION

In summary, we performed a systematic investigation of phase formation in CrFeCoNi solid solutions with the addition of nitrogen. DFT calculations of mixing energy ΔG were carried out with reference to three competing phases states: CrN, Fe-Ni-, and Co-rich. The mixing energy as a function of nitrogen concentration has a maximum at $x = 0.20$ – 0.25 , which explains the segregation in experimental films with $x = 0.22$ of nitrogen. The lower values of ΔG at $x \leq 0.10$ and $x \geq 0.25$ concentration of nitrogen can qualitatively explain the stabilization of single-phase structures in $(\text{CrFeCoNi})_{1-x}\text{N}_x$. The films undergo segregation when the nitrogen content in the film is sufficient to form CrN as reference phase. At $x = 0.20$, the competing reference phases are at their most stable states: ideal CrN and nitrogen-free Fe-Ni and Co. As a result, the mixing free energy has the highest value at $x = 0.20$. The configuration entropy contributes to stabilizing single-phase structures in $(\text{CrFeCoNi})_{1-x}\text{N}_x$ at high temperatures. The theoretically and experimentally obtained results on phase formation well corroborate each other. These results further aid in understanding the mechanical and electrical properties of

the films. The highest hardness was achieved on the film with multiple phases. This study provides a guideline for ceramic Cantor alloy-related systems and can assist researchers in the field when choosing deposition parameters to grow films with specified structures and properties.

The data supporting the findings of this study is available [33].

ACKNOWLEDGMENTS

The work was supported financially by the VINNOVA Competence Centre FunMat-II (Grant No. 2016–05156), the Swedish Government Strategic Research Area in Materials Science on Functional Materials at Linköping University (Faculty Grant SFO-Mat-LiU No. 2009 00971), the Knut and Alice Wallenberg foundation through the Wallenberg Academy Fellows program (KAW-2020.0196) and the Wallenberg Scholar Grant (KAW-2018.0194), the Swedish Foundation for Strategic research through the Future research leaders 6 program SSF-FFL 15–0290, and by the Swedish Research Council (VR) under Projects No.

2021–03826 and No. 2019–05403. The computations were enabled by resources provided by the Swedish National Infrastructure for Computing (SNIC) located at the National Supercomputer Centre (NSC) in Linköping, partially funded by the Swedish Research Council through Grant Agreement No. 2018–05973. Accelerator operation at Uppsala University was supported by Swedish Research Council VR-RFI (Contract No. 2019-00191). The Swedish Research Council and the Swedish Foundation for Strategic Research are acknowledged for access to ARTEMI, the Swedish National Infrastructure in Advanced Electron Microscopy (Grants No. 2021-00171 and No. RIF21-0026).

S.M.G.: Conceptualization, Experimental Investigation, Data curation, Formal analysis, Writing - original draft. B.M.: Conceptualization, Theoretical Investigation, Data curation, Formal analysis, Writing - original draft. G.N.: Experimen-

tal data curation, Formal analysis Writing - review and editing. E.N.T.: Experimental data curation, Formal analysis, Writing - review and editing. R.S.: Formal analysis, Writing - review and editing. R.B.: Experimental data curation, Formal analysis, Writing - review and editing. D.P.: Experimental data curation, Writing - review and editing, Funding acquisition. P.P.: Writing - review and editing, Funding acquisition. B.A.: Conceptualization, Theoretical Investigation, Supervision, Formal analysis, Writing - review and editing. I.A.A.: Project administration, Conceptualization, Supervision, Formal analysis, Writing - review and editing, Funding acquisition. A.L.F.: Conceptualization, Investigation, Supervision, Formal analysis, Writing - review and editing. P.E.: Project administration, Conceptualization, Supervision, Writing - review and editing, Funding acquisition.

- [1] A. J. B. Vincent, A study of three multicomponent alloys, B.Sc. Part II thesis, University of Sussex, UK, 1981.
- [2] B. S. Murty, J. W. Yeh, and S. Ranganathan, A brief history of alloys and the birth of high-entropy alloys, in *High Entropy Alloys* (Elsevier, Amsterdam, 2014), pp. 1–12.
- [3] B. Cantor, I. T. H. Chang, P. Knight, and A. J. B. Vincent, Microstructural development in equiatomic multicomponent alloys, *Mater. Sci. Eng. A* **375–377**, 213 (2004).
- [4] J. W. Yeh, S. K. Chen, S. J. Lin, J. Y. Gan, T. S. Chin, T. T. Shun, C. H. Tsau, and S. Y. Chang, Nanostructured high-entropy alloys with multiple principal elements: Novel alloy design concepts and outcomes, *Adv. Eng. Mater.* **6**, 299 (2004).
- [5] D. B. Miracle and O. N. Senkov, A critical review of high entropy alloys and related concepts, *Acta Mater.* **122**, 448 (2017).
- [6] E. P. George, D. Raabe, and R. O. Ritchie, High-entropy alloys, *Nat. Rev. Mater.* **4**, 515 (2019).
- [7] Y. Zhang, Y. J. Zhou, J. P. Lin, G. L. Chen, and P. K. Liaw, Solid-solution phase formation rules for multi-component alloys, *Adv. Eng. Mater.* **10**, 534 (2008).
- [8] C.-J. Tong, Y.-L. Chen, J.-W. Yeh, S.-J. Lin, S.-K. Chen, T.-T. Shun, C.-H. Tsau, and S.-Y. Chang, Microstructure characterization of $\text{Al}_x\text{CoCrCuFeNi}$ high-entropy alloy system with multiprincipal elements, *Metall. Mater. Trans. A* **36**, 881 (2005).
- [9] S. Guo, C. Ng, J. Lu, and C. T. Liu, Effect of valence electron concentration on stability of Fcc or Bcc phase in high entropy alloys, *J. Appl. Phys.* **109**, 103505 (2011).
- [10] U. Mizutani, The hume-rothery rules for structurally complex alloy phases, in *Surface Properties and Engineering of Complex Intermetallics* (2010), pp. 323–399.
- [11] S. A. Kube, S. Sohn, D. Uhl, A. Datye, A. Mehta, and J. Schroers, Phase selection motifs in high entropy alloys revealed through combinatorial methods: Large atomic size difference favors BCC over FCC, *Acta Mater.* **166**, 677 (2019).
- [12] M. C. Gao, J.-W. Yeh, P. K. Liaw, Y. Zhang *et al.*, Overview of high-entropy alloys, in *High-Entropy Alloys: Fundamentals and Applications* (Springer, Cham, 2016), pp. 1–19.
- [13] S. Yang, J. Lu, F. Xing, L. Zhang, and Y. Zhong, Revisit the VEC rule in high entropy alloys (HEAs) with high-throughput CALPHAD approach and its applications for material design-a case study with Al–Co–Cr–Fe–Ni system, *Acta Mater.* **192**, 11 (2020).
- [14] K. M. Youssef, A. J. Zaddach, C. Niu, D. L. Irving, and C. C. Koch, A novel low-density, high-hardness, high-entropy alloy with close-packed single-phase nanocrystalline structures, *Mater. Res. Lett.* **3**, 95 (2014).
- [15] E. Lewin, Multi-component and high-entropy nitride coatings—a promising field in need of a novel approach, *J. Appl. Phys.* **127**, 160901 (2020).
- [16] P. E. Blöchl, Projector augmented-wave method, *Phys. Rev. B* **50**, 17953 (1994).
- [17] G. Kresse and J. Furthmüller, Efficiency of *ab initio* total energy calculations for metals and semiconductors using a plane-wave basis set, *Comput. Mater. Sci.* **6**, 15 (1996).
- [18] G. Kresse and J. Furthmüller, Efficient iterative schemes for *ab initio* total-energy calculations using a plane-wave basis set, *Phys. Rev. B* **54**, 11169 (1996).
- [19] A. Zunger, S. H. Wei, L. G. Ferreira, and J. E. Bernard, Special Quasirandom Structures, *Phys. Rev. Lett.* **65**, 353 (1990).
- [20] B. L. Gyorffy, A. J. Pindor, J. Staunton, G. M. Stocks, and H. Winter, A first-principles theory of ferromagnetic phase transitions in metals, *J. Phys. F* **15**, 1337 (1985).
- [21] B. Alling, T. Marten, and I. A. Abrikosov, Effect of magnetic disorder and strong electron correlations on the thermodynamics of CrN, *Phys. Rev. B* **82**, 184430 (2010).
- [22] J. P. Perdew, K. Burke, and M. Ernzerhof, Generalized Gradient Approximation Made Simple, *Phys. Rev. Lett.* **77**, 3865 (1996).
- [23] H. Hellmann, Lebenslauf von hans hellmann, in *Hans Hellmann: Einführung in Die Quantenchemie: Mit biografischen Notizen von Hans Hellmann jr* (2015), pp. 3–15.
- [24] D. Ma, B. Grabowski, F. Körmann, J. Neugebauer, and D. Raabe, *Ab initio* thermodynamics of the CoCrFeMnNi high entropy alloy: importance of entropy contributions beyond the configurational one, *Acta Mater.* **100**, 90 (2015).
- [25] F. Körmann, A. A. H. Breidi, S. L. Dudarev, N. Dupin, G. Ghosh, T. Hickel, P. Korzhavyi, J. A. Muñoz, and I. Ohnuma, Lambda transitions in materials science: Recent advances in CALPHAD and first-principles modelling *Phys. Status Solidi B* **251**, 53 (2014).
- [26] See Supplemental Material at <http://link.aps.org/supplemental/10.1103/PhysRevMaterials.7.055002> for contains information

- regarding calculated structure and configuration entropy along with experimental details regarding metallic and nitrogen containing films.
- [27] T. Nishizawa and K. Ishida, The Co–Fe (Cobalt–Iron) system, *Bull. Alloy Phase Diagr.* **5**, 250 (1984).
- [28] A. le Febvrier, L. Landalv, T. Liersch, D. Sandmark, P. Sandstrom, and P. Eklund, An upgraded ultra-high vacuum magnetron-sputtering system for high-versatility and software-controlled deposition, *Vacuum* **187**, 110137 (2021).
- [29] P. Ström and D. Primetzhofer, Ion beam tools for nondestructive in-situ and in-operando composition analysis and modification of materials at the tandem laboratory in uppsala, *J. Instrum.* **17**, P04011 (2022).
- [30] M. Mayer, SIMNRA User's Guide, Max-Planck-Institut für Plasmaphysik, 1997.
- [31] M. K. Kini *et al.*, Nanocrystalline equiatomic CoCrFeNi alloy thin films: Are they single phase Fcc?, *Surf. Coatings Technol.* **410**, 126945 (2021).
- [32] A. K. Niessen and F. R. De Boer, The enthalpy of formation of solid borides, carbides, nitrides, silicides and phosphides of transition and noble metals, *J. Less-Common Met.* **82**, 75 (1981).
- [33] https://data.openmaterialsdb.se/crfenico_n/.